J. Fluid Mech. (2007), *vol.* 589, *pp.* 125–145.
doi:10.1017/S0022112007007872 Printed in the United Kingdom

Geometry of unsteady fluid transport during fluid–structure interactions

ELISA FRANCO[1], DAVID N. PEKAREK[2], JIFENG PENG[3] AND JOHN O. DABIRI[3,4]

[1]Control and Dynamical Systems, California Institute of Technology, Pasadena, CA 91125, USA

[2]Mechanical Engineering, California Institute of Technology, Pasadena, CA 91125, USA

[3]Bioengineering, California Institute of Technology, Pasadena, CA 91125, USA

[4]Graduate Aeronautical Laboratories, California Institute of Technology, Pasadena, CA 91125, USA
jodabiri@caltech.edu

(Received 7 November 2006 and in revised form 23 May 2007)

We describe the application of tools from dynamical systems to define and quantify the unsteady fluid transport that occurs during fluid–structure interactions and in unsteady recirculating flows. The properties of Lagrangian coherent structures (LCS) are used to enable analysis of flows with arbitrary time-dependence, thereby extending previous analytical results for steady and time-periodic flows. The LCS kinematics are used to formulate a unique, physically motivated definition for fluid exchange surfaces and transport lobes in the flow. The methods are applied to numerical simulations of two-dimensional flow past a circular cylinder at a Reynolds number of 200; and to measurements of a freely swimming organism, the *Aurelia aurita* jellyfish. The former flow provides a canonical system in which to compare the present geometrical analysis with classical, Eulerian (e.g. vortex shedding) perspectives of fluid–structure interactions. The latter flow is used to deduce the physical coupling that exists between mass and momentum transport during self-propulsion. In both cases, the present methods reveal a well-defined, unsteady recirculation zone that is not apparent in the corresponding velocity or vorticity fields. Transport rates between the ambient flow and the recirculation zone are computed for both flows. Comparison of fluid transport geometry for the cylinder crossflow and the self-propelled swimmer within the context of existing theory for two-dimensional lobe dynamics enables qualitative localization of flow three-dimensionality based on the planar measurements. Benefits and limitations of the implemented methods are discussed, and some potential applications for flow control, unsteady propulsion, and biological fluid dynamics are proposed.

1. Introduction

It is often of interest in fluid mechanics to quantify the exchange of mass, momentum, and energy between different regions of a flow. In many cases these mixing processes can be described in terms of specific kinematic boundaries in the flow, material surfaces that delineate fluid particles with distinct behaviours. These surfaces governing the exchange of fluid between different regions of the flow (hereafter referred to as *exchange surfaces*) can be identified in steady flows from inspection of streamlines derived from the Eulerian velocity field. In cases of steady flow, the exchange surface commonly manifests itself as a closed recirculation bubble that traps fluid particles over long convective time scales. Examples include the

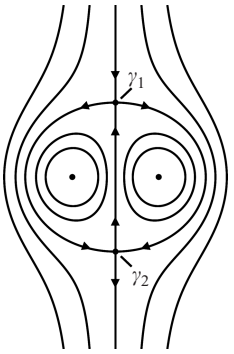

FIGURE 1. Schematic of manifolds for the recirculation bubble of a vortex pair. Fluid particle trajectories (i.e. streamlines in steady flow) that asymptote to the front stagnation point γ_1 as time $t \to \infty$ belong to the stable manifold of γ_1, whereas trajectories that asymptote to γ_1 as time $t \to -\infty$ belong to the unstable manifold of γ_1. The same considerations apply to γ_2.

laminar separation bubble over an airfoil at low Reynolds number (e.g. O'Meara & Mueller 1987) and the cardiovascular recirculation zone caused by an aneurysm (e.g. Faturaee & Amini 2003).

Knowledge of the geometry and kinematics of the exchange surfaces in a flow can be used to monitor the performance of a given fluid transport system or to improve its performance via flow control. Indeed, these flow kinematics can be a useful surrogate for the fluid dynamics (i.e. forces and moments) when they are difficult to evaluate directly. However, since the majority of flows of practical interest exhibit unsteadiness (time-dependence), streamline representations are of limited use for capturing the kinematics of the exchange surfaces.

The application of dynamical systems tools to fluid mechanics has enabled precise identification of exchange surfaces in unsteady flows that exhibit a well-defined temporal periodicity in the fluid motion. The theory governing fluid transport in time-periodic flows is now well developed and has been demonstrated in a variety of canonical systems including the oscillating vortex pair, isolated and leapfrogging vortex rings, and cylinder crossflow (e.g. Aref 1984; Rom-Kedar & Wiggins 1990; Rom-Kedar, Leonard & Wiggins 1990; Shariff, Leonard & Ferziger 1989, 2006; Shariff, Pulliam & Ottino 1991; Duan & Wiggins 1997; see Wiggins 2005 for an excellent review). In each case, the analysis relies on the identification of stable and unstable *manifolds*, which are the collection of fluid particle trajectories that asymptote to a point in the flow as time moves forward or backward, respectively. Figure 1 illustrates this concept for the exchange surface that encloses the cores of a vortex pair. The manifolds of interest for defining the exchange surface are typically those of the stagnation and/or separation points in the flow, as shown in the figure.

A geometric definition of the governing fluid exchange surface based on the manifolds in the flow is in general not unique; multiple definitions can be derived from the same set of stable and unstable manifolds. For simple manifolds in time-periodic flows there is typically a single definition for the exchange surface that stands out because of the relative simplicity of the flow geometry that it suggests (Rom-Kedar *et al.* 1990). In the case of the steady vortex pair in figure 1, the elliptical boundary connecting γ_1 and γ_2 most appropriately defines the exchange surface.

In unsteady flows with arbitrary time-dependence, however, it is often difficult to distinguish between the many possible definitions of the exchange surface that can be

constructed from the stable and unstable manifolds (whose definition is appropriately modified to account for the lack of periodicity in the flow). The level of difficulty in applying a particular exchange surface definition to the flow can vary substantially from one definition to the next and even for the same definition evaluated at different times during the temporal evolution of the flow (Malhotra & Wiggins 1998). Hence, computing transport rates in aperiodic flows currently relies on the implementation of *ad hoc* transport definitions that are specific to the particular flow being investigated.

The goal of this paper is to propose and demonstrate an unambiguous, robust, and physically motivated geometric definition of fluid exchange surfaces that can be easily applied to compute transport rates in arbitrary unsteady aperiodic flows. The proposed definition has several distinguishing features. First, the evolution of the defined exchange surfaces qualitatively resembles the processes of entrainment and detrainment that are observed in flow visualizations using a passive flow marker (e.g. Sturtevant 1981; Yamada & Matsui 1978). This is not true of alternative definitions. Second, in the limit of time-periodic flow, the proposed definition is identical to the definition traditionally selected on the basis of aesthetic merits in previous studies (e.g. Rom-Kedar *et al.* 1990). Third, in the limit of steady flow, the proposed definition is identical to the exchange surface that would be identified in a streamline plot of the flow (e.g. Milne-Thompson 1968).

In the place of stable and unstable manifolds, which are a valid concept for strictly time-periodic systems, we identify analogous Lagrangian coherent structures (LCS) in the flows to be investigated. The LCS share many of the properties of manifolds (see the following sections for details), but can be computed based on a finite-time record of the flow, which need not be time-periodic (Haller 2000, 2001, 2002; Shadden, Lekien & Marsden 2005; Shadden, Dabiri & Marsden 2006; Green, Rowley & Haller 2007). In addition, an important benefit of LCS for flow analysis is its objectivity, or invariance under linear transformations of frame (Haller 2005). By constructing the proposed exchange surface definition using LCS, it too is made objective.

We apply the proposed exchange surface analysis to study fluid–structure interactions. Whereas much of the classical study of mixing has focused on isolated vortical structures and unbounded flows, most practical flows involve the presence of solid structures that either bound the flow or are immersed within it. The flow created by a freely swimming jellyfish provides the main application in this paper. The selection of this model system is motivated by the fact that it exhibits aperiodic flow despite the relative simplicity of its body shape and motion, as shown in figures 2 and 3. Muscle contraction reduces the volume of the subumbrellar cavity (i.e. the region underneath its umbrella-shaped body), resulting in a net downward flux of fluid. The motion of the lower margin of the bell generates vortex rings of opposite rotational sense during the contraction and relaxation phases of the swimming cycle (see figure 2). These vortices act to entrain fluid from above the animal into the subumbrellar cavity, where the feeding and sensory apparatus of the animal are located. Despite the approximate periodicity of the swimming motion, inspection of the flow created by the animal indicates that it is indeed aperiodic in time. Further, since the animal does not swim at constant velocity, a periodic flow cannot be constructed by any Galilean transformation of frame.

Instantaneous streamlines of the flow field measured by using digital particle image velocimetry (DPIV) indicate local entrainment of fluid from above the animal into the subumbrellar cavity during the entire swimming cycle. Simultaneously, a net downward momentum flux propels the animal forward (figure 3). Although

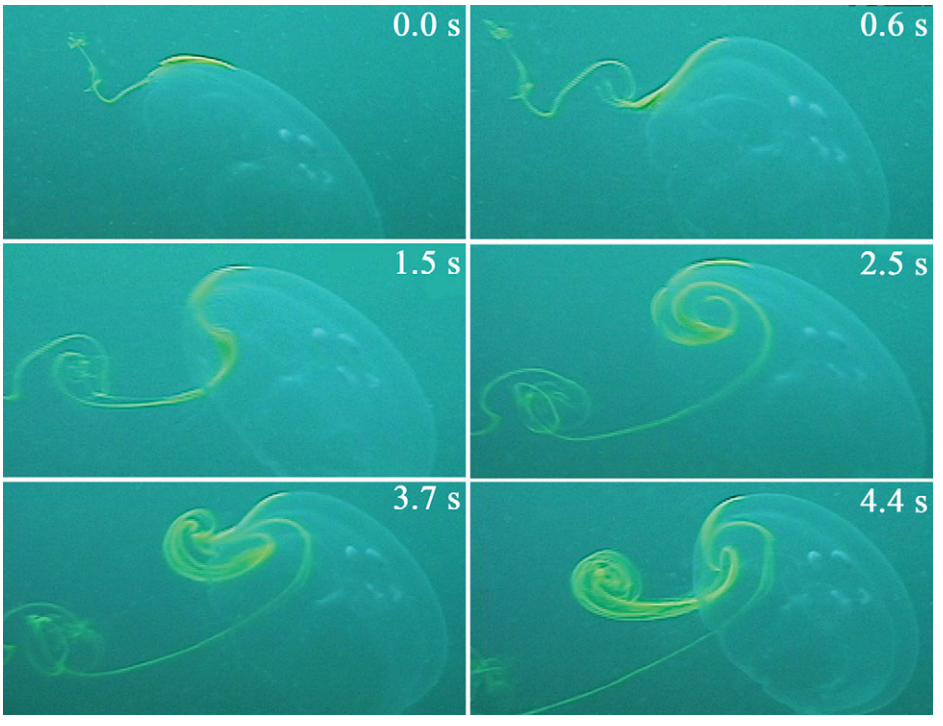

FIGURE 2. Dye visualization of jellyfish vortex wake (Dabiri *et al.* 2005). Time series shows vortices of clockwise and anticlockwise rotational sense generated during the contraction and relaxation phases of the swimming cycle, respectively. Bell diameter is 10 cm.

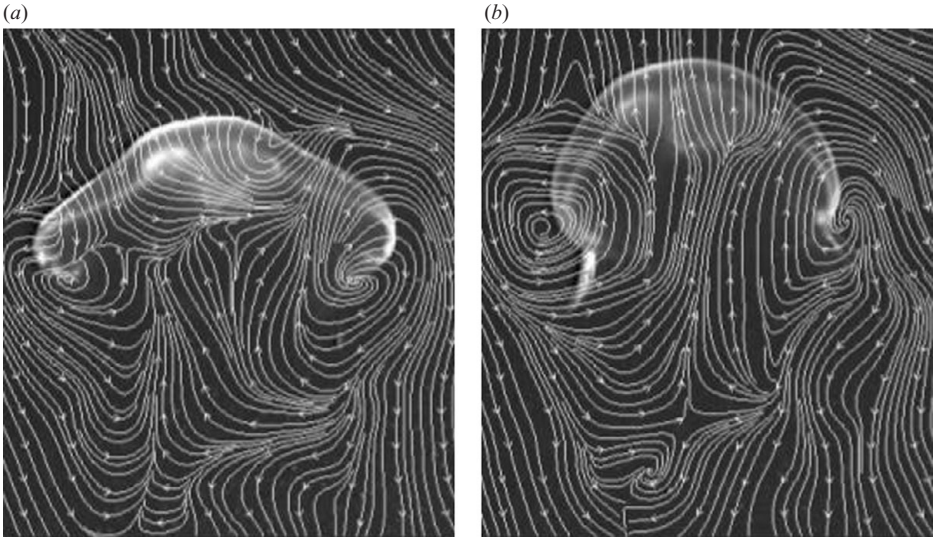

FIGURE 3. Instantaneous streamlines of flow around a jellyfish as it swims vertically. (*a*) End of relaxation phase of swimming cycle. (*b*) End of contraction phase of swimming cycle. Bell diameter is 10 cm

the flow features in figure 3 lead one to anticipate the existence of exchange surfaces surrounding the animal, these surfaces are not apparent in the instantaneous streamline plots. We will show that the present methods are sufficient to define

and quantify the exchange surfaces governing fluid transport induced by the animal swimming motions

Shadden *et al.* (2006) have previously computed LCS analogous to stable manifolds for a free-swimming animal, the same species as studied here. However, in that work the LCS was computed for the purpose of demonstrating that the LCS behave as material lines as predicted by theory. There is no quantification of the associated fluid transport therein or elsewhere. Indeed, there could be no discussion of fluid transport previously because (i) the LCS analogous to unstable manifolds have not previously been computed for this flow and (ii) as mentioned above, an empirical treatment of LCS in the context of aperiodic exchange surfaces, the goal of this paper, has not been addressed previously to our knowledge.

We note that the present study is restricted to planar sections of a three-dimensional flow. Limitations of the two-dimensional measurements are inferred in this paper by comparing properties of the measured LCS evolution with previous theoretical considerations of two-dimensional LCS kinematics. In addition, we apply the methods of analysis to direct numerical simulations of two-dimensional flow past a circular cylinder at a Reynolds number of 200. This canonical flow allows comparison between classical perspectives on fluid–structure interactions (e.g. vortex shedding) and the geometric viewpoint taken in this paper. In addition, the two-dimensional flow enables validation of the inferences made in the jellyfish study. Salman *et al.* (2007) recently computed LCS for a more complex two-dimensional bluff-body configuration. Although the mechanism of fluid transport is described in that paper, quantitative measurements of transport rates are not presented.

The paper is organized as follows: § 2 presents the foundational dynamical systems concepts, including a review of the mechanism of unsteady fluid transport via exchange surfaces. This is followed by a presentation of the proposed definition of exchange surfaces in aperiodic flow and examples of its implementation in a simple vortex model. We prove that the proposed definition satisfies the classical manifold-intersection ordering criterion governing time-periodic flows. The utility of LCS for computing the exchange surfaces in flows with arbitrary time-dependence is then presented. Finally, the methods used to extract LCS and exchange surfaces from the jellyfish flow and cylinder crossflow are described in this section. Section 3 reports results obtained from the case study of the freely swimming animals showing both the measured LCS evolution and the associated transport rates computed using the proposed exchange surface definition. A sensitivity analysis is conducted to determine the robustness of the fluid transport measurements to perturbations away from the specific exchange surface definition selected for study here. In addition, flow dimensionality inferred from the manifold kinematics is compared with divergence calculations of the corresponding Eulerian velocity fields. These conclusions are supported by the results of the numerical study of cylinder crossflow, which is also presented in this section. The paper concludes with a discussion of the benefits and limitations of the developed methods and suggestions for potential applications in § 4.

2. Analytical and experimental methods

2.1. *Definition and analysis of exchange surfaces*

As described by Malhotra & Wiggins (1998), the manifold geometry illustrated in figure 1 is unique to a limited set of steady or quasi-steady flows. In most situations of practical relevance, the time-dependent hyperbolic trajectories $\gamma_1(t)$ and $\gamma_2(t)$ will be perturbed, e.g. due to an external strain field (Rom-Kedar *et al.* 1990) or ellipticity of

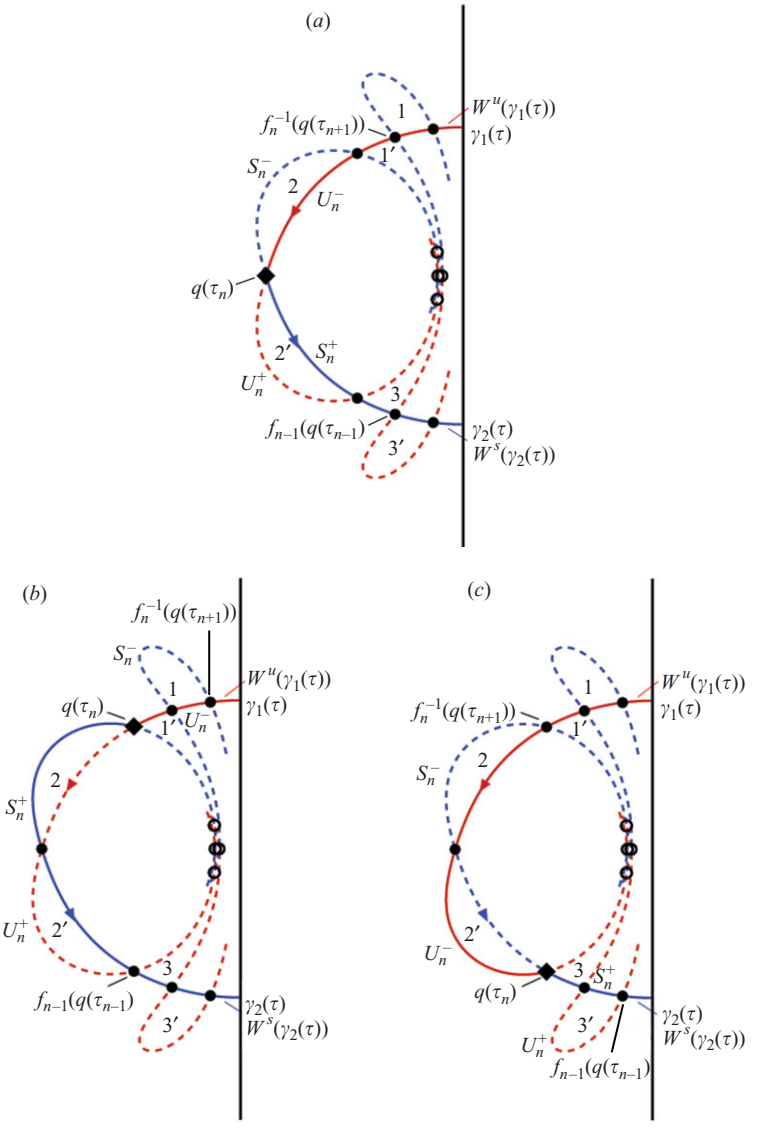

FIGURE 4. (*a*) Schematic of perturbed recirculation bubble analogous to the unperturbed steady case shown in figure 1. Symmetric right half of flow omitted for clarity. Blue curve, stable manifold of $\gamma_2(\tau)$; red curve, unstable manifold of $\gamma_1(\tau)$; filled circles, p.i.p.s.; open circles, non-p.i.p.s.; filled diamond, b.i.p. Solid curves indicate the exchange surface derived from the stable and unstable manifolds. Fluid is transported through consecutively numbered lobes as the manifolds evolve in time. Unprimed indices indicate fluid transport into the recirculation region. Primed indices indicate fluid transport out of the recirculation region. Segment lengths S_n^-, S_n^+, U_n^-, and U_n^+ are used to evaluate the b.i.p. criterion in equation (2.1) and are defined in the text. (*b*) Resulting flow geometry using adjacent p.i.p. closer to $\gamma_1(t)$ as the b.i.p. (*c*) Resulting flow geometry using adjacent p.i.p. closer to $\gamma_2(t)$ as the b.i.p.

the vortex cores (Shariff *et al.* 1989, 2006). In these cases, the heteroclinic trajectories connecting $\gamma_1(t)$ and $\gamma_2(t)$ will break and exhibit spatial oscillations, as illustrated in figure 4(*a*) for the left-hand side of the symmetric flow. The stable and unstable manifolds will then intersect, forming *lobes*. Formally, these lobes are defined as areas

delimited by segments of the stable and unstable manifolds and by *primary intersection points* (p.i.p.s) of the stable and unstable manifolds. Guckenheimer & Holmes (1983) and Malhotra & Wiggins (1998) define p.i.p.s as follows:

CONDITION 2.1. *At each time instant τ, p.i.p.s $p(\tau)$ are points such that:*

$$p(\tau) \in W^u(\gamma_1(\tau)) \cap W^s(\gamma_2(\tau)),$$

$$\textit{and} \quad [W^u(\gamma_1(\tau)), p(\tau)] \cap [W^s(\gamma_2(\tau)), p(\tau)] = p(\tau),$$

where $W^s(\gamma_2(\tau))$ denotes the stable manifold of $\gamma_2(\tau)$ at time τ, $W^u(\gamma_1(\tau))$ denotes the unstable manifold of $\gamma_1(\tau)$, and the bracketed expressions denote the segments of these manifolds connecting the respective hyperbolic trajectory, $\gamma_1(\tau)$ or $\gamma_2(\tau)$, to $p(\tau)$; see figure 4(a). The first statement requires that the p.i.p. lies on both the stable and the unstable manifold. The second statement requires that a p.i.p. is the only intersection of the segments $[W^u(\gamma_1(\tau)), p(\tau)]$ and $[W^s(\gamma_2(\tau)), p(\tau)]$ that connect the p.i.p. to $\gamma_1(\tau)$ and $\gamma_2(\tau)$, respectively. For example, the filled circles in figure 4(a) indicate intersections that define p.i.p.s, whereas the open circles are not p.i.p.s.

The above definition implies that each lobe, defined by the union of two neighbouring p.i.p.s and the neighbouring segments of the stable and unstable manifolds, is a region of trapped fluid, because the manifolds are material lines in the flow. As a consequence, lobe areas of a two-dimensional incompressible flow must remain constant despite deformation and advection of the manifolds that occurs due to the time-dependent nature of the flow.

The fact that the manifolds in the flow are material lines implies the following rules regarding the temporal evolution of the flow (Guckenheimer & Holmes 1983; Malhotra & Wiggins 1998):

Rule 1: Maintenance of order under time evolution. $W^u(\gamma_1(\tau))$ and $W^s(\gamma_2(\tau))$ are one-dimensional curves at any time τ. An ordering of points can therefore be defined on, e.g., $W^s(\gamma_2(\tau))$ as follows: for any two points $p(\tau)$, $q(\tau) \in W^s(\gamma_2(\tau))$, $p(\tau) <_s q(\tau)$ if $p(\tau)$ is closer to $\gamma_2(\tau)$ along the arclength of the curve $W^s(\gamma_2(\tau))$. As the flow evolves temporally, $p(\tau + t) = f_\tau^{\tau+t}(p(\tau))$ and $q(\tau + t) = f_\tau^{\tau+t}(q(\tau))$ will still belong to $W^s(\gamma_2(\tau + t))$, and $p(\tau + t) <_s q(\tau + t)$, where f is an orientation-preserving diffeomorphism between two points in time. In the present context, $f_\tau^{\tau+t}$ maps the flow from time τ to time $\tau + t$.

Rule 2: Invariance of intersections. If at time τ, $W^u(\gamma_1(\tau))$ and $W^s(\gamma_2(\tau))$ intersect, then they intersect at all times. This follows from the invariance properties of the manifolds, i.e. the fact that the manifolds behave as material lines in the flow.

The p.i.p.s travel along the stable manifold of $\gamma_2(t)$ as the flow evolves. Concomitantly, the lobes defined by the p.i.p.s deform and stretch, transporting the fluid particles trapped in the lobe across a (still undefined) exchange surface formed by the intersection of the stable and unstable manifolds. Since our goal is to quantify fluid transport from empirical observations of lobe evolution, we must define this time-varying exchange surface that will be computed along with the lobe areas. To this end, the following criterion for the choice of an exchange surface is proposed, respecting the theoretical p.i.p. ordering Rule 1 and Rule 2.

Following the work of Malhotra & Wiggins (1998, p. 415), let us first consider the evolution of $W^u(\gamma_1(\tau))$ and $W^s(\gamma_2(\tau))$ over a strictly increasing time sequence $\mathscr{T} \triangleq \{\tau_1, \tau_2, \ldots, \tau_{n-1}, \tau_n, \tau_{n+1}, \ldots\}$, $\forall\, n \in \mathbb{Z}$. As previously noted, at each arbitrary time τ_n, points $p(\tau_n)$ on the manifolds are mapped to new points $p(\tau_{n+1}) = f_n(p(\tau_n))$,

where for notational simplicity the flow map that advects fluid particles forward in time will henceforth be denoted as f_n.

To define the exchange surface, we want to identify a sequence of *boundary intersection points* (b.i.p.s) $q(\tau_n)$. The b.i.p.s will in turn define the exchange surface (a curve in two dimensions) $\mathscr{B}(\tau_n)$, as the union of two segments: $[W^s(\gamma_2(\tau_n)), q(\tau_n)]$, which is the arclength from the b.i.p. $q(\tau_n)$ to the hyperbolic trajectory $\gamma_2(\tau_n)$ travelling on the stable manifold; and $[W^u(\gamma_1(\tau_n)), q(\tau_n)]$, which is the arclength from $q(\tau_n)$ to the $\gamma_1(\tau_n)$ along the unstable manifold. Therefore the desired exchange surface is defined as $\mathscr{B}(\tau_n) \triangleq [W^s(\gamma_2(\tau_n)), q(\tau_n)] \bigcup [W^u(\gamma_1(\tau_n)), q(\tau_n)]$. Flow crossing the exchange surface defined by this bounding curve from time τ_n to time τ_{n+1} is identically the fluid transport that occurs due to the lobe dynamics.

The sequence of b.i.p.s used to define the exchange surface should satisfy the following ordering (Malhotra & Wiggins 1998):

CONDITION 2.2. *At each time instant τ_n, the chosen b.i.p. $q(\tau_n)$ must satisfy:*

$$q(\tau_n) <_s f_n^{-1}(q(\tau_{n+1})), \quad \forall n \in \mathbb{Z}$$

where the notation $<_s$ indicates the ordering on the stable manifold of $\gamma_2(t)$, using the arclength distance of the candidate points from $\gamma_2(t)$, as defined by Rule 1.

By itself, this condition does not specify a unique b.i.p. among the multiplicity of p.i.p.s; it merely constrains the direction of the sequence of b.i.p.s, such that the location of the current b.i.p. should be closer to $\gamma_2(\tau_n)$ than the current location of the next b.i.p. This prevents the b.i.p.s from approaching γ_2 as $n \to \infty$. Since the b.i.p. is not uniquely defined by this criterion, the exchange surface is also not uniquely defined. For example, the b.i.p. selected in figure 4(*a*) (filled diamond) results in an exchange surface given by the union of the solid red and blue curves. However, one could also select the p.i.p above (figure 4*b*), or below (figure 4*c*) this intersection point, and that new b.i.p could also satisfy Condition 2.2 while producing a different geometry for the exchange surface. For the exchange surface defined in figure 4(*b*), fluid enters the recirculation region as lobe 1 evolves into lobe 2, instead of during the $2 \to 3$ lobe evolution as in figure 4(*a*). However, fluid exits the recirculation region during the same $1' \to 2'$ lobe evolution as in the exchange surface defined in figure 4(*a*). Conversely, the exchange surface in figure 4(*c*) differs from figure 4(*a*) in the process of fluid detrainment from the recirculation region, but has an identical entrainment process.

Current practice is to select the p.i.p. giving the exchange surface that most closely resembles an equivalent unperturbed flow (e.g. Rom-Kedar *et al.* 1990); in the present case, comparison of figure 4(*a*) with figure 1 shows that the point denoted by the filled diamond is most appropriate from this perspective. Yet, for the majority of unsteady flows, there is no unperturbed reference state with which one can compare in order to determine an appropriate definition for the exchange surface (e.g. Salman *et al.* 2007). This ambiguity limits comparisons of unsteady fluid transport between systems, or even in the same system examined at different times during its temporal evolution.

We propose the following criterion for the b.i.p. sequence:

Criterion for boundary intersection points. At each time instant τ_n, choose as a boundary intersection point the intersection $q(\tau_n)$ for which

$$\left.\begin{aligned} S_n^+ < U_n^+, \\ S_n^- > U_n^-, \end{aligned}\right\} \tag{2.1}$$

where we define $S_n^+ \triangleq [q(\tau_n), f_{n-1}(q(\tau_{n-1}))]$, which is the segment on the stable manifold of $\gamma_2(\tau_n)$ connecting $q(\tau_n)$ and $f_{n-1}(q(\tau_{n-1}))$ (in words, the latter term represents the current location of the previous b.i.p.). Similarly, $U_n^+ \triangleq [q(\tau_n), f_{n-1}(q(\tau_{n-1}))]$, i.e. the segment with identical endpoints but on the unstable manifold of $\gamma_1(\tau_n)$. The definitions of S_n^- and U_n^- follow as: $S_n^- \triangleq [f_n^{-1}(q(\tau_{n+1})), q(\tau_n)]$ taking the segment on $W^s(\gamma_2(\tau_n))$, and $U_n^- \triangleq [f_n^{-1}(q(\tau_{n+1})), q(\tau_n)]$ on $W^u(\gamma_1(\tau_n))$. In words, the term $f_n^{-1}(q(\tau_{n+1}))$ represents the current location of the next b.i.p.

Qualitatively speaking, this criterion identifies the b.i.p. as the p.i.p. connecting the segments of the stable and unstable manifolds with least deformation from an equivalent unperturbed state. In other words, we define fluid transport according to evaluation of the length relationships in equation (2.1). An ancillary benefit of the exchange surface defined by this choice of b.i.p. is that it presents the smallest temporal shape oscillation. Since the stable manifold of $\gamma_2(\tau_n)$ becomes increasingly deformed as it approaches $\gamma_1(\tau_n)$ and the unstable manifold of $\gamma_1(\tau_n)$ becomes increasingly deformed as it approaches $\gamma_2(\tau_n)$, the b.i.p. will be located away from both $\gamma_1(\tau_n)$ and $\gamma_2(\tau_n)$. In the case of the vortex model in figure 4(*a*), the b.i.p. defined by the present criterion is in fact equidistant from both hyperbolic trajectories. Furthermore, this choice of b.i.p. coincides with the one that would be chosen in order to define an exchange surface that most closely resembles the bounding streamline of the analogous unperturbed steady flow in figure 1 (cf. Rom-Kedar *et al.* 1990). The benefit of the proposed criterion is that it can be applied to flows with arbitrary unsteadiness where there does not exist an analogous steady flow for comparison.

Using the vortex model in figure 4(*a*), let us consider the qualitative evolution of the exchange surface defined by the present b.i.p criterion. Although the criterion is evaluated on the discrete time sequence τ_n, the real flow is continuous in time. Hence, for closely spaced time sequences, the choice of b.i.p may not change at each τ_n. In this case, the b.i.p. will be advected along $W^s(\gamma_2(\tau_n))$ while maintaining its identity over successive time instants τ_n, and the corresponding exchange surface (i.e. the curve $[W^s(\gamma_2(\tau_n)), q(\tau_n)] \bigcup [W^u(\gamma_1(\tau_n)), q(\tau_n)]$) will deform. This deformation will continue until the current b.i.p. no longer satisfies the aforementioned criterion in equation (2.1). At this time, a p.i.p. (i.e. a different fluid particle) closer to $\gamma_1(\tau_n)$ will become the new b.i.p. and the exchange surface will be redefined accordingly. The pictorial evolution suggested by the present b.i.p. criterion will be shown in detail in the following section.

The described b.i.p. criterion is objective (i.e. frame-invariant) and has a practical relevance: given an empirical set of lobes evolving in time, it facilitates the definition of the exchange surface directly from observations of segment lengths along the stable and unstable manifolds. It also guarantees that the aforementioned theoretical requirements (i.e. Guckenheimer & Holmes 1983; Malhotra & Wiggins 1998) are fully satisfied.

It is straightforward to prove the following Lemma:

LEMMA 2.1. *The criterion defined above for the choice of b.i.p. sequence satisfies Condition* 2.2.

Proof. It is sufficient to first notice that all points on $W^s(\gamma_2(\tau_n)) \bigcap W^u(\gamma_1(\tau_n))$ at time τ_{n+1} will have moved closer to $\gamma_2(\tau_{n+1})$ in the arclength sense; intersection points travelling toward γ_2 will therefore decrease their distance from the neighbouring intersection points on the stable manifold. Conversely, lobe area preservation imposes stretching of the corresponding arclength segments on the unstable manifold (i.e. a filamentation process).

Now at time τ_{n+1}, we choose $q(\tau_{n+1})$ such that $S^-_{n+1} > U^-_{n+1}$ and $S^+_{n+1} < U^+_{n+1}$, as the criterion requires. By definition, $S^+_{n+1} = [q(\tau_{n+1}), f_n(q(\tau_n))] = f_n(S^-_n)$, and $f_n(S^-_n) < S^-_n$ since segments are shrinking on the stable manifold. Therefore we have that $q(\tau_n) <_s f_n^{-1} q(\tau_{n+1})$.

It is worth noting that the behaviour of $q(\tau_n)$ given by the proposed criterion is not compatible with any other ordering than the one imposed by Condition 2.2. *Ab absurdo*, let us assume that our criterion is applied:

$$S^-_{n+1} = f_n(S^+_n) > f_n(U^+_n) = U^-_{n+1}, \tag{2.2}$$

where now $q(\tau_n) >_s f_n^{-1}(q(\tau_{n+1}))$. Always by the chosen criterion, we have

$$\left.\begin{aligned} &S^+_n < U^+_n, \\ &f_n(S^+_n) < S^+_n, \\ &f_n(U^+_n) > U^+_n, \end{aligned}\right\} \tag{2.3}$$

and therefore $f_n(S^+_n) < S^+_n < U^+_n < f_n(U^+_n)$, which contradicts (2.2).

This Lemma could also be proved using the orientation-preserving property of flow maps. There exist other b.i.p. criteria that will satisfy Condition 2.2, producing exchange surfaces such as the alternatives illustrated in figure 4(b, c). The present criterion however, based on comparison of segment lengths, is intuitive and easily applicable to experimentally determined manifolds with very irregular shapes, where lobes are not always clearly discernible to the observer. Furthermore, the present b.i.p. criterion can be implemented in the cases of finite or infinitely many p.i.p.s, as long as there exists a sufficient number of p.i.p.s to evaluate the b.i.p. criterion stated in equation (2.1).

2.2. *Definition and properties of Lagrangian coherent structures*

Given the preceding developments, we are left with the task of extracting the stable and unstable manifolds from measurements or computations of the flow. In steady and time-periodic flows, it may suffice to examine streamlines or a Poincaré map, respectively, in order to determine the manifold geometry. However, these tools are of limited use in flows with arbitrary time-dependence, e.g. aperiodicity. Here, we make use of the finite-time Lyapunov exponents (FTLE; also referred to as *direct Lyapunov exponents* in the literature) of the velocity field.

The Lyapunov exponent describes the rate of extension of a line element advected in the flow. The line elements that experience the most rapid extension are proposed to straddle (i.e. possess endpoints on opposite sides of) a material line that acts as a barrier to fluid particle transport (Haller 2000, 2002; Shadden *et al.* 2005).

Restricting our attention to a two-dimensional domain D, consider the following system that describes the flow:

$$\left.\begin{aligned} &\dot{x}(t; x_0, t_0) = u(x(t; x_0, t_0), t), \\ &x(t_0; x_0, t_0) = x_0, \end{aligned}\right\} \tag{2.4}$$

where $x_0 \in D$ is the initial position and t_0 is the initial time of the fluid particle trajectory. We will assume that the Eulerian velocity field $u(x, t)$ is at least $\mathscr{C}^0$ in time and $\mathscr{C}^2$ in space. The flow map satisfying equation (2.4) will be denoted as $f^t_{t_0}(x_0) = x(t; x_0, t_0)$. This solution satisfies existence and uniqueness properties, and is $\mathscr{C}^1$ in time and $\mathscr{C}^3$ in space.

The Cauchy–Green deformation tensor C generated by the flow map $f^t_{t_0}(x_0)$ can be evaluated over a finite time interval T, giving a measure of how particles are advected

under the action of the flow:

$$C \triangleq [\nabla f_{t_0}^{t_0+T}(x)]^* \nabla f_{t_0}^{t_0+T}(x), \tag{2.5}$$

where C depends on x_0, t_0 and T; $[\,]^*$ denotes the adjoint (transpose) of $[\,]$. As shown previously (Haller 2000, 2002; Shadden *et al.* 2005), denoting the largest eigenvalue of C as $\lambda_{max}(C)$, the FTLE is defined as

$$\sigma_{t_0}^{T} = \frac{1}{|T|} \ln \sqrt{\lambda_{max}(C)}. \tag{2.6}$$

The aforementioned assumptions on the vector field imply that the field $\sigma_{t_0}^{T}$ is $\mathscr{C}^1$ in time and $\mathscr{C}^2$ in space.

LCS can be defined as a ridge line of the function σ. Intuitively, a ridge line is a curve normal to which the topography is a local maximum. There are two precise definitions of a ridge line introduced by Shadden *et al.* (2005); here we adopt the second of these, called the second-derivative ridge.

Definition 1. A second-derivative ridge of σ is a curve $c(s)$ whose tangent vector $\mathrm{d}c/\mathrm{d}s$ is parallel to $\nabla\sigma((c(s))$ and whose Hessian $\Sigma(n, n) < 0$, where n is the unit vector normal to $c(s)$.

At every time t, the LCS is defined as a second derivative ridge of $\sigma_{t_0}^{T}(x)$, $x \in D$. When fluid particle trajectories are integrated forward in time (i.e. $T > 0$), *repelling* LCS are revealed. These LCS are said to be repelling because as fluid particles approach the hyperbolic trajectory (e.g. γ_2) along the repelling LCS, particles on either side of the LCS are strongly repelled. Hence, repelling LCS can indicate the geometry of stable manifolds. Conversely, backward-time integration of fluid particle trajectories ($T < 0$) reveals *attracting* LCS, along which fluid particles on either side of the LCS are repelled as they move toward the hyperbolic trajectory (e.g. γ_1) in *backward* time. Attracting LCS can indicate the geometry of unstable manifolds. Physically, both attracting and repelling LCS are material lines separating regions of flow that exhibit different dynamics, such as the recirculation regions that are of present interest.

2.3. *Empirical evaluation of the exchange surface definition*

To demonstrate the utility of the methods described in the previous section, the unsteady, aperiodic flow generated by a free-swimming *Aurelia aurita* jellyfish was analysed. The flow map of the fluid advection around the animal is clearly not available in closed form, providing an opportunity to investigate the proposed methods in a relatively simple geometry that exhibits complex, coupled fluid–structure interactions.

Details of the experimental methods were similar to a recent study involving the same species of animal (Shadden *et al.* 2006). DPIV measurements of the symmetry plane of the animal were collected for several consecutive swimming cycles executed in a large tank. The animal swam vertically in a rectilinear fashion away from the tank walls; hence, all of the observed flow phenomena were induced by the swimming motions of the animal.

To support the jellyfish studies, the fluid transport analysis methods were also applied to direct numerical simulations of two-dimensional flow past a circular cylinder at Reynolds number $Re = 200$ based on the free-stream velocity and cylinder diameter (Taira & Colonius 2007). Unlike the jellyfish flow, the cylinder crossflow is time-periodic. In addition, the well-known kinematics of that flow field (e.g. vortex

shedding) should provide a useful comparison with the present perspective based on exchange surfaces.

The measured or computed time series of Eulerian velocity fields was input to an in-house code (Peng & Dabiri 2007) in order to compute the LCS. The integration duration T was ± 13 s for the jellyfish flows (a shorter backward-time duration was required toward the beginning of the measurements due to limited backward-time data initially) and ± 1.5 vortex shedding cycles for the cylinder crossflow. A second in-house code analysed the LCS curves in order to identify p.i.p.s, b.i.p.s, and the corresponding exchange surfaces. Our approach toward these calculations is as follows:

(i) The repelling (i.e. forward time) and attracting (i.e. backward time) LCS are both broken into several short, linear segments that approximate the LCS curves.

(ii) For each segment of the repelling LCS, a rectangular neighbourhood of interest is defined, centred at the midpoint of the segment and enclosing the segment.

(iii) Linear segments of the attracting LCS that possess an endpoint within the neighbourhood of interest are isolated. The size of rectangular neighbourhood relative to the length of each segment is sufficiently large that it is impossible for any segment of the attracting LCS without an endpoint inside the rectangular neighbourhood to intersect the repelling LCS segment in question.

(iv) For each of the attracting LCS segments with an endpoint inside the rectangular neighbourhood, the intersection point of the line containing it and the line containing the repelling LCS segment in question is calculated. In the case of parallel segments, this intersection point does not exist.

(v) A Boolean check is performed to determine if the coordinates of the intersection point lie on both the repelling and attracting LCS segments. If so, this point is in fact an intersection of the two LCS.

The algorithm was verified manually for the data presented in this paper and was shown to function correctly. Upon proper identification of the set of intersection points between the attracting and repelling LCS, p.i.p.s and b.i.p.s were determined based on their respective definitions given in the previous section. The lobe structure of the jellyfish flow was such that for every time instant considered, every LCS intersection point satisfied the p.i.p. criteria. This was not the case for the cylinder crossflow. In both cases, the b.i.p. criterion in equation (2.1) was evaluated unambiguously at each time step.

With the p.i.p.s and b.i.p.s recorded, the LCS arclengths that define the lobes and exchange surface were isolated from the full set of LCS data. The area of the ith lobe was calculated with the following formula for the area of a polygon, based on Green's Theorem in the plane:

$$A(L_i)(t) = \frac{1}{2}\sum_{j=0}^{n-1}[x_j(t)y_{j+1}(t) - x_{j+1}(t)y_j(t)], \tag{2.7}$$

where x_j and y_j are the first and second components respectively for the beginning and ending points of the jth segment defining lobe L_i.

3. Results

Figure 5 plots the results of the transport analysis at four instants during the jellyfish swimming cycle. The LCS curves analogous stable and unstable manifolds are shown in yellow and green respectively. The p.i.p.s are denoted by open red circles, whereas the b.i.p.s are denoted by filled red circles. Based on these b.i.p.s,

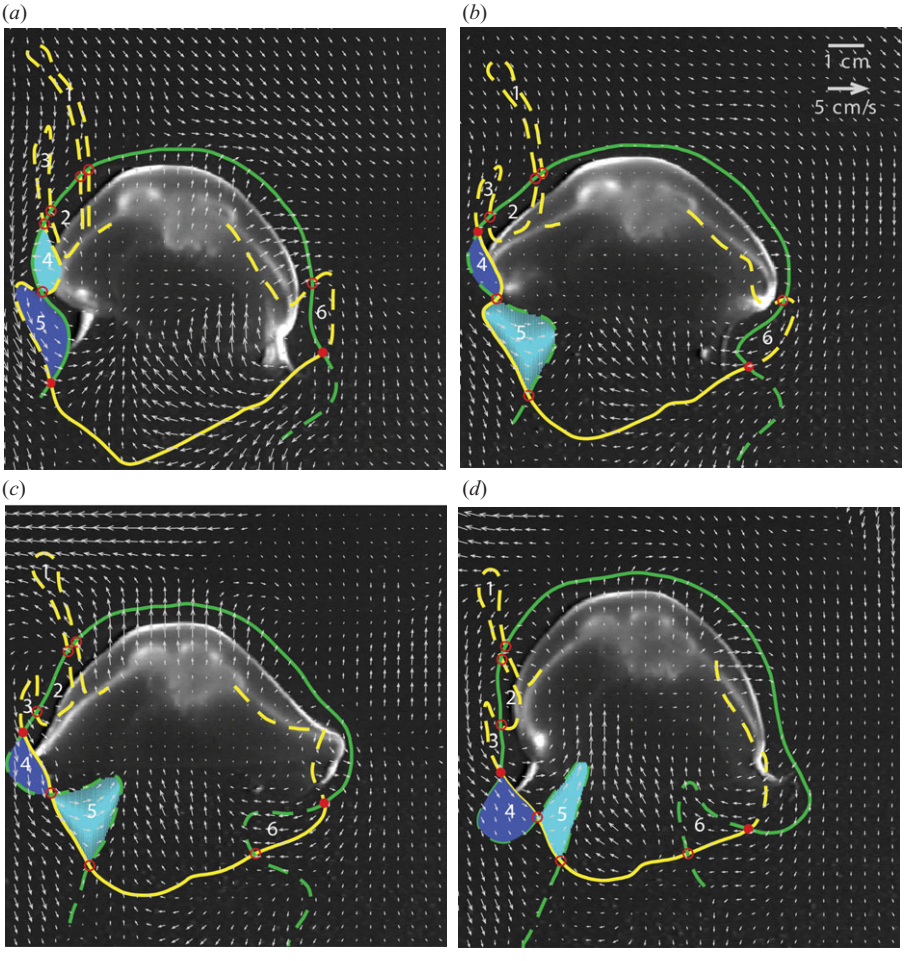

FIGURE 5. Forward- and backward-time LCS surrounding a freely swimming jellyfish at four instants during a swimming cycle. (*a*) $t = 0$, (*b*) $t = 1.07$ s, (*c*) $t = 2.13$ s, and (*d*) $t = 3.27$ s; yellow, forward-time LCS; green, backward-time LCS; open red circles, p.i.p.s; filled red circles, b.i.p.s; segments of the stable and unstable manifolds that constitute the exchange surface are indicated in solid lines, the remainder of the manifolds in dashed lines. Lobes are numbered consecutively. Light blue, lobe inside recirculation region; dark blue, lobe outside recirculation region.

the exchange surface is defined as the union of the solid portions of the yellow and green curves. The lobes formed by the p.i.p.s and adjacent segments of the LCS are numbered sequentially from lobe 1 upstream of the animal to lobes 5 and 6 in the wake. Based on the exchange surface definition, lobe 4 (light blue) is initially located inside the recirculation region, whereas lobe 5 (dark blue) is located outside. The temporal evolution of the flow illustrates the transport of fluid across the exchange surface by the lobes during the swimming cycle. We note that although the existence of transversely intersecting LCS is suggested by previous theoretical work (e.g. Guckenheimer & Holmes 1983; Malhotra & Wiggins 1998), these interesting flow kinematics are impossible to detect from inspection of the velocity field.

Equally interesting are the exchange surfaces observed in the canonical cylinder crossflow (figure 6). This flow, previously studied by using Poincaré maps (Shariff *et al.*

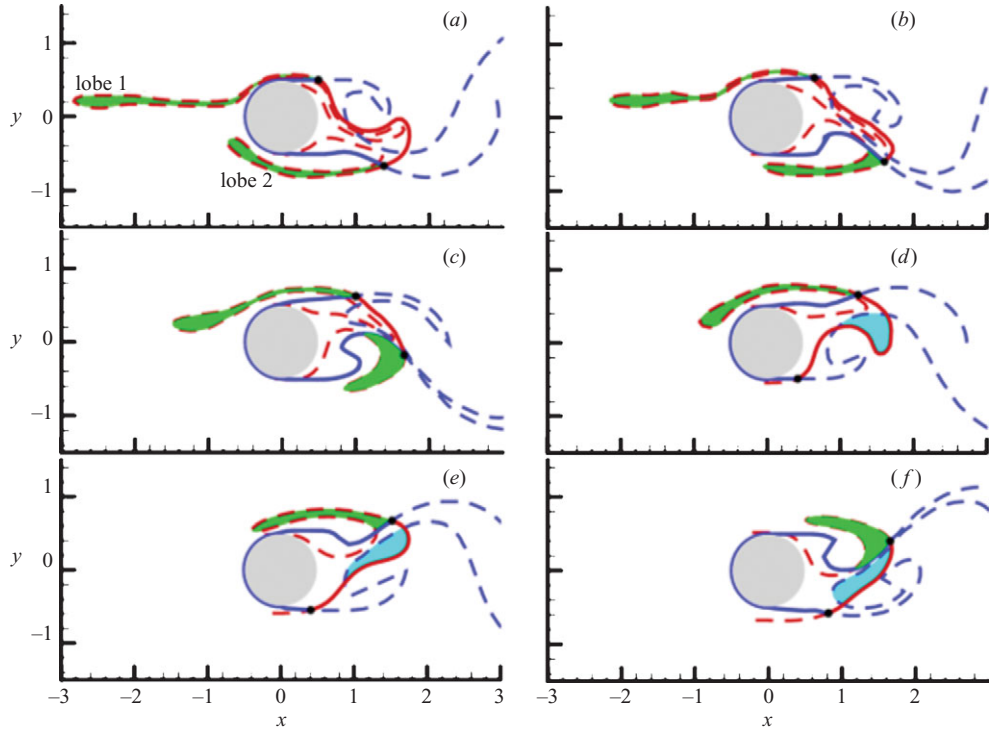

FIGURE 6. Forward- and backward-time LCS surrounding a circular cylinder at six instants during a vortex shedding cycle. Red, forward-time LCS; blue, backward-time LCS; filled black circles, b.i.p.s; segments of the stable and unstable manifolds that constitute the exchange surface are shown in solid lines, the remainder of the manifolds in dashed lines. Fluid inside two lobes is shown: green, lobe outside recirculation region; light blue, lobe inside the recirculation region. The circular cylinder is shown in grey.

1991), consists of two long, narrow lobes defined primarily by the repelling LCS (red curve) that propagate from upstream toward the rear of the cylinder. The fluid carried by these lobes crosses the exchange surface determined by the b.i.p.s (solid red/blue curves and filled black circles, respectively) and enters a well-defined recirculation region behind the cylinder. The lower lobe crosses the exchange surface first, as indicated by its colour change from green to light blue. This fluid will eventually cross the exchange surface again as it is detrained downstream via interaction with the attracting LCS (blue curve). As in the jellyfish flow, inspection of the velocity or vorticity field would not reveal this mass transport geometry. However, one does get a sense for the locations where vortex shedding occurs by examining the kinematics of the attracting LCS, especially where the this curve folds back onto itself. This is not by coincidence: passive scalars, such as a dye used to visualize the flow, will tend to align with the attracting LCS (Shariff *et al.* 1989; Voth, Haller & Gollub 2002).

Previous analytical studies of time-periodic flows have demonstrated that the rate of fluid transport into the region bounded by the exchange surface is directly proportional to the area of the lobes (in two dimensions; Rom-Kedar *et al.* 1990 and Shariff *et al.* 2006). Figure 7 plots the temporal evolution of the area of each of the lobes identified in figure 5. In addition to the direct area measurement, we also present calculations of an equivalent lobe volume based on an assumption of axisymmetry in the flow. These calculations were made by assigning an axis of

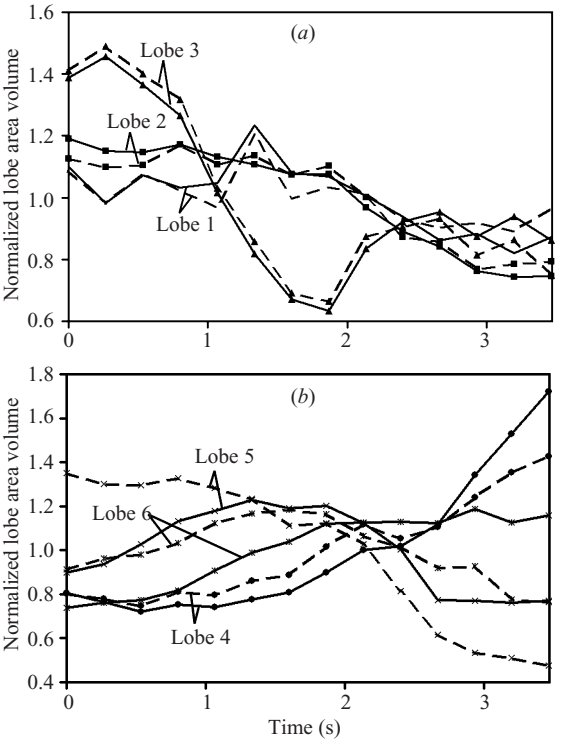

FIGURE 7. Temporal evolution of normalized lobe area (solid lines) and lobe volume (dashed lines) during a cycle of jellyfish swimming. Normalized values represent the instantaneous lobe area (volume) divided by the time-averaged area (volume) of that lobe over the swimming cycle. (*a*) Lobes 1–3. (*b*) Lobes 4–6.

symmetry that coincides with the symmetry axis of the animal. To compare these calculations with the lobe area measurements, we plot both quantities normalized by the average value of that quantity over the swimming cycle. The average value is taken separately for each lobe. Differences between the behaviour of the lobe area and lobe volume are small for lobes above the animal and become more severe for lobes near the lower margin. This is a direct consequence of the radial lobe motion that occurs near the lower margin, which appears in the additional $O(r)$ dependence of the volume calculation relative to the area calculation.

Since the number of lobes that can be extracted from the flow is dependent on the integration time T used to compute the LCS (i.e. more of the manifold is revealed as the integration is carried out for longer times; cf. Haller 2000, 2002; Shadden *et al.* 2005), it is useful to consider the average lobe area as opposed to the total area of all of the lobes in order to study fluid transport. In a two-dimensional flow, lobe area preservation requires that the ratio of the total area of all of the lobes to the area of any individual lobe is exactly equal to the number of lobes in the flow (Rom-Kedar *et al.* 1990; Malhotra & Wiggins 1998). Hence, in this case the behaviour of the average lobe area is sufficient to characterize all of the lobe dynamics. Figure 8(*a*) plots the ratio of the average lobe area (volume) to the area (volume) of the circulation region. The average lobe area is approximately 2 % of the recirculation region area; the average lobe volume is approximately 13 % of the recirculation region volume. One of these lobe volumes (in three dimensions) or two of these lobe areas (one per

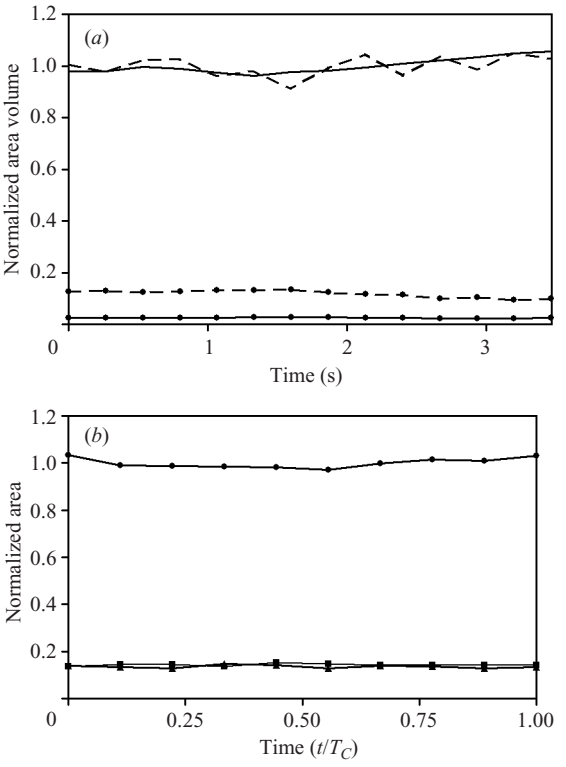

FIGURE 8. (*a*) Temporal evolution of the area (volume) of the average lobe and the recirculation region for the jellyfish flow. Normalized values represent the instantaneous area (volume) divided by the time-averaged area (volume) of the recirculation region over the swimming cycle. Solid lines, area; dashed lines, volume; lines with dots, average lobe; lines without dots, recirculation region. (*b*) Temporal evolution of the area of each lobe and the recirculation region for the cylinder crossflow. Normalized values represent the instantaneous area divided by the time-averaged area of the recirculation region over a vortex shedding cycle of duration T_C. Filled circles, recirculation region; filled squares, lobe 1; filled triangles, lobe 2.

side of the animal in two dimensions) is added and removed from the recirculation region per swimming cycle. Since the total recirculation region does not change appreciably in size over time (figure 8*a*), the lobe dynamics give an indication of the fluid turnover rate within the recirculation region. For the jellyfish flow this turnover rate is on the order of 10% per swimming cycle. A similar analysis can be performed for the cylinder crossflow, as shown in figure 8(*b*). In this case, two lobes (one above and one below the cylinder centreline) are added and removed from the recirculation region during each vortex shedding cycle of duration T_C. The corresponding fluid turnover rate is approximately 14% per vortex shedding cycle.

We now examine the sensitivity of the results to the choice of the b.i.p. that defines the exchange surface and associated recirculation region for the jellyfish flow. Figure 9 compares the temporal evolution of the area bounded by the current exchange surface definition to the corresponding areas enclosed by modified exchange surfaces. These modified surfaces are defined using the adjacent p.i.p.s that are either directly above or below the current b.i.p. (cf. figure 4*b*, *c*). In cases where the current b.i.p. has no adjacent p.i.p. below it (e.g. figure 5*a*), the current b.i.p. is used in the comparison. The data are shown for the four time instants in figure 5. The results indicate

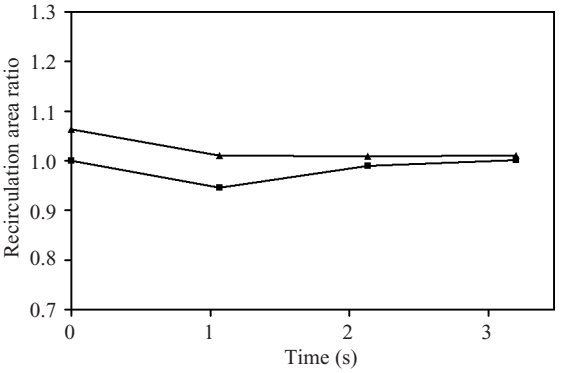

FIGURE 9. Ratio of the area bounded by modified exchange surfaces defined using adjacent p.i.p. above (filled triangles) or below (filled squares) the actual b.i.p., respectively, to the area bounded by the original exchange surface. Data points correspond to the images in figure 5.

that the measurements are relatively robust to changes of the b.i.p. to its nearest neighbour p.i.p. The use of the adjacent p.i.p. below the current b.i.p. results in a slight underestimate of the area enclosed by the exchange surface. Conversely the use of the adjacent p.i.p. above the current b.i.p. results in a slight overestimate. This relative insensitivity suggests that despite the discontinuous shifts in b.i.p. that occur as the b.i.p. criterion is evaluated on the temporally evolving LCS curves, physically consistent results can be obtained and used for quantitative comparison of fluid transport systems.

The temporal variation of the lobe areas in figure 7 is in violation of the known behaviour of two-dimensional lobes in incompressible flow. A major source of this spurious result is the three-dimensionality of the flow, which is not captured by the two-dimensional DPIV measurements. In principle, the amount of time-dependence exhibited by each lobe area can therefore be used as a measure of the local flow three-dimensionality. For example, it can be inferred from the relatively constant area of lobes 1 and 2 that the flow in their vicinity (upstream of the animal) is nearly two-dimensional. By contrast, the flow near lobes 5 and 6 (in the vortical wake) exhibits three-dimensionality that appears in the transient behaviour of the corresponding lobe areas. As would be expected, the spatial transition between two- and three-dimensionality is gradual, given the even spatial distribution of lobes in the streamwise direction from lobe 1 to lobes 5 and 6.

Quantitatively, figure 10 shows that the standard deviation of the normalized lobe areas plotted in figure 7 increases from approximately 10% upstream of the animal to over 30% in the wake. The locations of two- and three-dimensionality in the flow, i.e. upstream and in the wake, respectively, match physical intuition for the flow around a self-propelled animal in quiescent surroundings. These locations are also consistent with previous dye visualizations of flow generated by the same animal species (Dabiri *et al.* (2005)).

Some of the area variation is due to error in determining the position of the LCS from the FTLE field. The numerical simulations of cylinder crossflow enable us to quantify this error, since that flow is two-dimensional by definition. As seen in figures 8(*b*) and 10, the lobes in this purely two-dimensional flow exhibit an area variation of approximately 4% over a vortex shedding cycle. This area variation is wholly attributable to error in LCS identification since no three-dimensionality

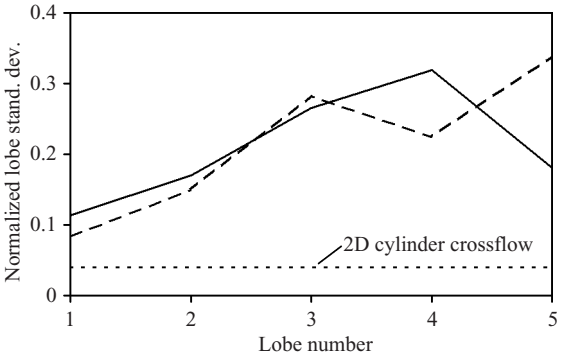

FIGURE 10. Standard deviation of normalized lobe area as a function of lobe number. Solid line, lobe area; dashed line, lobe volume. Standard deviation of two-dimensional cylinder crossflow lobes is included for reference.

exists. These results suggest that the flow upstream of the animal may be closer to two-dimensional than the magnitude of the standard deviation in lobe area implies.

Finally, figure 11 plots the divergence of the velocity field shown in figure 5(*a*). Deviations from zero divergence suggest three-dimensionality in the flow. The locations of highest velocity field divergence (i.e. in the downstream wake) are consistent with the regions of maximum lobe area variation, supporting the notion that lobe area evolution can be examined as a metric for flow three-dimensionality. The divergence calculation has the added benefit of point-wise evaluation of flow dimensionality, whereas the lobe examination only gives information regarding average behaviour within a lobe. However, in cases where lobe evolution has already been computed for transport measurements, the area variation can complement existing metrics with no added computational effort.

4. Discussion

The geometry of flow elucidated by these methods shows some striking differences from conventional Eulerian perspectives such as velocity and vorticity fields. Indeed, much of the fluid transport geometry is hidden when one examines the flows studied in this paper using those metrics. As suggested by Shariff *et al.* (1989), the attracting (backward-time) LCS shows qualitative similarity to what would be observed in the flow using a passive scalar such as dye to mark the fluid particles. However, there appears to be no analogous visualization to produce the repelling (forward-time) LCS structure. The repelling LCS structure revealed in the cylinder crossflow provides an interesting and unconventional perspective on that canonical flow. The transport role of the upstream lobes may be a useful target for manipulation in various flow control applications. Notably, despite the fact that the Reynolds number ($Re = 200$) is in the regime of periodic vortex shedding, there exists a well-defined, time-varying recirculation region at the base of the cylinder that is revealed by the present methods. The role of such regions in external flows of this kind should receive greater attention in the future. We hypothesize that similar structures will exist in other bluff body flows as well as in structures of importance in aero- and hydrodynamics. The recent results of Salman *et al.* (2007) support this conclusion.

The case study of jellyfish swimming provided a test of the methods in a flow with more complex fluid–structure interactions and temporal aperiodicity. Despite the

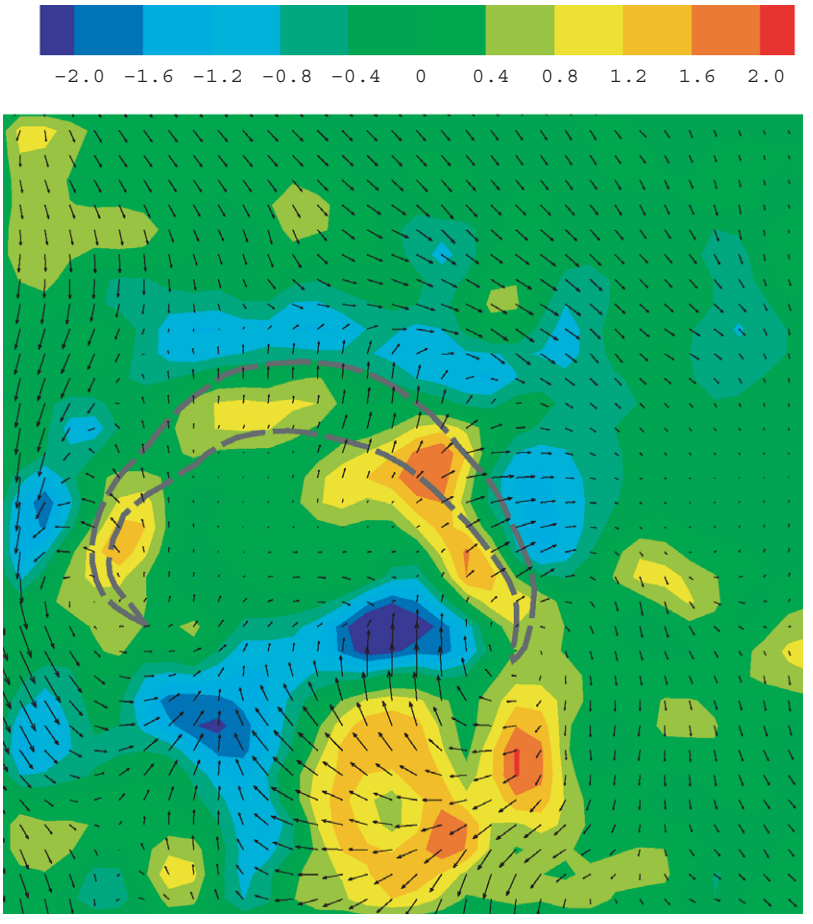

FIGURE 11. Divergence of DPIV velocity field surrounding a freely swimming jellyfish at $t = 0$, cf. figure 5(*a*). Locations of non-zero divergence indicate three-dimensional flow. Animal position is shown in dashed outline.

increased complexity, the lobe dynamics predicted in the simple model vortex system appeared in this flow as well. By extracting the geometry of fluid transport, it was possible to quantify the mass transport that occurs concomitantly with momentum transport during self-propulsion. This mass transport has biological significance because local environmental sensing is a vital capability for many self-propelled organisms like the jellyfish. By increasing the rate of fluid turnover within the recirculation region, the animal is able to more effectively deduce the properties (e.g. chemical cues) of the surrounding fluid.

The fluid turnover metric can be similarly useful for identifying the precise effect of various flow control strategies (e.g. blowing and suction) on the surrounding fluid. For example, the upstream lobes observed in figure 6 indicate exactly which fluid incident on the body in the flow is actually affected by the control strategies. Moreover, the magnitude of the fluid turnover rate can indicate the duration of the interaction between that fluid and the body, when coupled with statistical methods (e.g. Rom-Kedar *et al.* 1990; Shariff *et al.* 1991; Duan & Wiggins 1997).

Measurements of unsteady propulsion can benefit from the present methods, as they suggest the possibility of computing unsteady mass flux induced by the propulsor. The

present tools can be especially useful where the propulsors generate an external flow (e.g. flapping foils or undulating bodies), in which case the mass flux can be difficult to estimate. Krueger (2006) has shown that measurements of this unsteady mass flux combined with an estimate of the mechanical power expended by a system can be used to compute propulsive efficiency without making an assumption of quasi-steady flow, as must be done to compute an equivalent Froude efficiency. Hence, the concepts described here can enable comparison of propulsive performance in swimming and flying organisms or in engineered propulsion systems that are unsteady.

Finally, although three-dimensional LCS and lobe structure is beyond the scope of the present work, three-dimensional flows are fully amenable to the present treatment. In those cases, the intersection points are replaced by intersection lines, and lobe areas become lobe volumes. The resulting exchange surfaces will then become truly three-dimensional. That development will provide valuable new insight into many of the flows under investigation in fluid dynamics.

The authors acknowledge insightful discussions with S. C. Shadden, J. E. Marsden, K. Shariff, very helpful suggestions from the manuscript referees, and funding from the NSF Biological Oceanography Program (OCE-0623475 to J.O.D.).

REFERENCES

Aref, H. 1984 Stirring by chaotic advection. *J. Fluid Mech.* **143**, 1–21.

Dabiri, J. O., Colin, S. P., Costello, J. H. & Gharib, M. 2005 Flow patterns generated by oblate medusan jellyfish: field measurements and laboratory analyses. *J. Expl Biol.* **208**, 1257–1265.

Duan, J. & Wiggins, S. 1997 Lagrangian transport and chaos in the near wake of the flow around an obstacle: a numerical implementation of lobe dynamics. *Nonlinear Proc. Geophys.* **4**, 125–136.

Fatouraee, N. & Amini, A. A. 2003 Regularization of flow streamlines in multislice phase-contrast MR imaging. *IEEE Trans. Medical Imaging* **22**, 699–709.

Green, M., Rowley, C. W. & Haller, G. 2007 Detection of Lagrangian coherent structures in three-dimensional turbulence. *J. Fluid Mech.* **572**, 111–120.

Guckenheimer, J. & Holmes, P. J. 1983 *Nonlinear Oscillations, Dynamical Systems, and Bifurcations of Vector Fields*. Springer.

Haller, G. 2000 Lagrangian coherent structures and mixing in two-dimensional turbulence. *Physica* D **147**, 352–370.

Haller, G. 2001 Lagrangian structures and the rate of strain in a partition of two-dimensional turbulences. *Phys. Fluids* **13**, 3368–3385.

Haller, G. 2002 Lagrangian coherent structures from approximate velocity data. *Phys. Fluids* **14**, 1851–1861.

Haller, G. 2005 An objective definition of a vortex. *J. Fluid Mech.* **525**, 1–26.

Krueger, P. S. 2006 Measurement of propulsive power and evaluation of propulsive performance from the wake of a self-propelled vehicle. *Bioinsp. Biomim.* **1**, S49–S56.

Malhotra, N. & Wiggins, S. 1998 Geometric structures, lobe dynamics, and lagrangian transport in flows with aperiodic time-dependence with applications to Rossby wave flow. *J. Nonlinear Sci.* **8**, 401–456.

Milne-Thompson, M. 1968 *Theoretical Hydrodynamics*. Dover.

O'Meara, M. M. & Mueller, T. J. 1987 Laminar separation bubble characteristics on an airfoil at low Reynolds numbers. *AIAA J.* **25**, 1033–1041.

Peng, J. & Dabiri, J. O. 2007 A potential-flow, deformable-body model for fluid-structure interactions with compact vorticity: application to animal swimming measurements. *Exps. Fluids* DOI: 10.1007/S00348-007-0315-1

Rom-Kedar, V., Leonard, A. & Wiggins, S. 1990 An analytical study of transport, mixing and chaos in an unsteady vortical flow. *J. Fluid Mech.* **214**, 347–394.

Rom-Kedar, V. & Wiggins, S. 1990 Transport in two-dimensional maps. *Arch. Rat. Mech. Anal.* **109**, 239–298.

Salman, H., Hesthaven, J. S., Warburton, T. & Haller, G. 2007 Predicting transport by Lagrangian coherent structures with a high-order method. *Theor. Comput. Fluid Dyn.* **21**, 39–58.

Shadden, S. C., Dabiri, J. O. & Marsden, J. E. 2006 Lagrangian analysis of fluid transport in empirical vortex ring flows. *Phys. Fluids* **18**, 047105.

Shadden, S. C., Lekien, F. & Marsden, J. E. 2005 Definition and properties of Lagrangian coherent structures from finite-time Lyapunov exponents in two-dimensional aperiodic flows. *Physica* D **212**, 271–304.

Shariff, K., Leonard, A. & Ferziger, J. H. 1989 Dynamics of a class of vortex rings. *NASA Tech. Mem.* 102257.

Shariff, K., Leonard, A. & Ferziger, J. H. 2006 Dynamical systems analysis of fluid transport in time-periodic vortex ring flows. *Phys. Fluids* **18**, 047104.

Shariff, K., Pulliam, T. H. & Ottino, J. M. 1991 A dynamical systems analysis of kinematics in the time-periodic wake of a circular cylinder. *Lectuces in Applied Mathematics*, vol. 28 (ed. E. L. Allgower, K. Georg & R. Miranda). pp. 613–646. Springer.

Sturtevant, B. 1981 Dynamics of turbulent vortex rings. *AFOSR-TR-81-0400,* available from Defense Technical Information Service, Govt. Accession. No. AD-A098111, Fiche N81-24027.

Taira, K. & Colonius, T. 2007 The immersed boundary method: a projection approach. *J. Comput. Phys.*, submitted.

Voth, G. A., Haller, G. & Gollub, J. P. 2002 Experimental measurements of stretching fields in fluid mixing. *Phys. Rev. Lett.* **88**, 254501.

Wiggins, S. 2005 The dynamical systems approach to Langrangian transport in oceanic flows. *Annu. Rev. Fluid Mech.* **37**, 295–328.

Yamada, H. & Matsui, T. 1978 Preliminary study of mutual slip-through of a pair of vortices. *Phys. Fluids* **21** 292–294.